# Response of type-II superconductors subjected to parallel rotating magnetic fields

Antonio Perez-Gonzalez and John R. Clem
*Ames Laboratory—United States Department of Energy and Department of Physics, Iowa State University, Ames, Iowa 50011*
(Received 14 December 1984)

A general critical-state model including the effects of both flux-line cutting and flux pinning is used for calculating **B**-, **J**-, and **E**-field distributions during the approach to the quasisteady state of a type-II superconducting slab subjected to a parallel rotating magnetic field. Three initial magnetic configurations (diamagnetic, paramagnetic, and nonmagnetic) are considered. It is shown that, depending upon sample parameters and magnetic history, multiple-zone structures develop inside the superconductor. It is also shown that, regardless of the specimen's magnetic history, flux-line-cutting $B$ consumption leads to a final state in which $B$ has a diamagnetic profile near the surface of the specimen. The relation of these calculations to the pioneering experiments of LeBlanc and co-workers is discussed.

## I. INTRODUCTION

In a previous paper,[1] we stated that in order to explain the experimental results[2–4] in type-II superconductors subjected to parallel magnetic fields that slowly rotate relative to the specimen, one must include flux-line-cutting effects in the theory of the static and dynamic magnetic behavior of these materials. In that paper we presented a general critical-state model using the theory of flux-line-cutting losses of Ref. 5 and used it in calculating the behavior of a type-II superconducting slab subjected to a rotating or oscillating applied magnetic field parallel to the flat surfaces.

Several surprising effects were observed in the experiments performed by LeBlanc and co-workers.[2–4] At the beginning of rotation, the magnitude of the magnetic flux density inside the sample decreased as if vortices were expelled against the Lorentz force, and diamagnetic profiles developed near the surfaces of the specimen. With further rotation, the fronts of these diamagnetic profiles penetrated deeper into the sample until either they reached the middle of the sample or $B$ was first brought to zero. In the latter case, the sample was divided into two types of regions: an inner, trapped-flux region where the vortices remained fixed relative to the specimen and no dissipation occurred, and outer, active regions adjoining the surfaces where the vortices moved relative to the sample and dissipation occurred. In the former case, the active regions included the entire specimen. These experiments were done beginning with four different initial magnetic configurations, nonmagnetic, diamagnetic, paramagnetic, and hybrid, which depended on the previous magnetic history of the sample.

In this paper we discuss the time evolution of the currents and the magnetic and electric fields, starting from three of the four initial magnetic states mentioned above and developing into the quasisteady state. As asserted before, regardless of the initial distribution $\mathbf{B}(x,0)$, the magnitude of the flux density $B(x,t)$ near the surface ($x=0$) evolves with time towards a quasisteady-state diamagnetic profile, $B(x)=B_0(1-x/x_0)$, in a dissipative region of thickness $x_d=\min(x_0,x_m)$. Here $x_0$ is the distance from the surface at which $B$ is or would be reduced from $B_0$ to zero, and $x_m$ is the middle of the sample. This effect is a consequence of Faraday's law written in the form

$$\frac{\partial B}{\partial t}+\frac{\partial j_{Bx}}{\partial x}=-\mu_0 J_{\parallel}E_{\parallel}/B\ , \tag{1}$$

which describes how flux-line cutting consumes $B$. Here $j_{Bx}=E_{\perp}=Bv_x$, and $J_{\parallel}$, $J_{\perp}$, $E_{\parallel}$, and $E_{\perp}$ are the parallel and perpendicular components, with respect to the local **B** field, of the current **J** and the electric field **E**, respectively.

In this paper we use the same notation as in Ref. 1 for referring to different zones. In a $T$ zone, only flux transport occurs ($E_{\perp}\neq 0$, $E_{\parallel}=0$); in a $C$ zone, only flux cutting occurs ($E_{\parallel}\neq 0$, $E_{\perp}=0$); in a $CT$ zone, both flux cutting and transport occur ($E_{\parallel}\neq 0$, $E_{\perp}\neq 0$); and in an $O$ zone, neither flux cutting nor flux transport occurs ($E_{\parallel}=0$, $E_{\perp}=0$). We also use subscripts $+$ and $-$ to denote the signs of the corresponding electric fields; i.e., a $C_-T_+$ zone is a zone in which flux-line cutting occurs with $E_{\parallel}<0$ and flux transport occurs with $E_{\perp}>0$.

In Sec. II we write down the basic equations of the general critical-state model. In the remainder of the paper we examine each of the initial configurations: Sec. III, diamagnetic initial state; Sec. IV, paramagnetic initial state; and Sec. V, nonmagnetic initial state. We show that, depending upon several specimen-dependent parameters, multiple-zone regimes can develop. We also show that, independent of magnetic history, flux-line-cutting $B$ consumption leads to a final state in which either $B$ has a diamagnetic profile or there are diamagnetic shoulders close to the sample surfaces and a frozen-in core of vortices in the middle of the sample. Finally, in Sec. VI we summarize our results, compare them to those of the empirical model of Refs. 2–4, and discuss possible extensions of the present theory.

 

## II. BASIC EQUATIONS

We consider, as in Ref. 1, a high-$\kappa$ irreversible type-II superconducting infinite slab with surfaces at $x=0$ and $x=X=2x_m$, to which we apply an external magnetic induction $\mathbf{B}_s(t)=\mu_0\mathbf{H}_s(t)=B_0\hat{\boldsymbol{\alpha}}_s(t)$ of fixed magnitude $B_0$ but changing direction,

$$\hat{\boldsymbol{\alpha}}_s=\hat{\mathbf{y}}\sin\alpha_s+\hat{\mathbf{z}}\cos\alpha_s \ . \tag{2}$$

For simplicity we assume $\mathbf{B}=\mu_0\mathbf{H}$ inside the sample, and we write $\mathbf{B}=B\hat{\boldsymbol{\alpha}}$ where $B=|\mathbf{B}|$ and

$$\hat{\boldsymbol{\alpha}}=\hat{\mathbf{y}}\sin\alpha+\hat{\mathbf{z}}\cos\alpha \ . \tag{3}$$

We also assume that the boundary conditions at $x=0$ and $x=X$ are $B=B_0$ and $\alpha=\alpha_s$. Then from Ampere's and Faraday's laws we obtain $\mathbf{J}=J_{||}\hat{\boldsymbol{\alpha}}+J_{\perp}\hat{\boldsymbol{\beta}}$, where

$$\hat{\boldsymbol{\beta}}=\hat{\boldsymbol{\alpha}}\times\hat{\mathbf{x}}=\hat{\mathbf{y}}\cos\alpha-\hat{\mathbf{z}}\sin\alpha \ , \tag{4}$$

$$J_{||}=\mu_0^{-1}B\frac{\partial\alpha}{\partial x} \ , \tag{5}$$

$$J_{\perp}=-\mu_0^{-1}\frac{\partial B}{\partial x} \ ; \tag{6}$$

and $\mathbf{E}=E_{||}\hat{\boldsymbol{\alpha}}+E_{\perp}\hat{\boldsymbol{\beta}}$, where

$$\frac{\partial E_{||}}{\partial x}=B\frac{\partial\alpha}{\partial t}+E_{\perp}\frac{\partial\alpha}{\partial x} \ , \tag{7}$$

$$\frac{\partial E_{\perp}}{\partial x}=-\frac{\partial B}{\partial t}-E_{||}\frac{\partial\alpha}{\partial x} \ . \tag{8}$$

Combining Eqs. (5) and (8), we obtain Eq. (1).

Because the same external field is applied to both surfaces, $\mathbf{B}$ has the symmetry $\mathbf{B}(x,t)=\mathbf{B}(X-x,t)$. Henceforth we shall examine only the half-thickness $0\leq x\leq x_m=X/2$.

As stated in Ref. 1, metastable stationary distributions of $B$ ($E_{\perp}=0$) and $\alpha$ ($E_{||}=0$) are such that

$$|J_{\perp}|\leq J_{c\perp}(B) \tag{9}$$

and

$$|J_{||}|\leq J_{c||}(B) \ , \tag{10}$$

respectively, where $J_{c\perp}$ ($J_{c||}$) is a function describing the transverse (longitudinal) critical current density at the threshold for depinning (onset of flux-line cutting) in the vortex array. Using Eq. (5), we can rewrite Eq. (10) as

$$\left|\frac{\partial\alpha}{\partial x}\right|\leq k_{c||}(B) \ , \tag{11}$$

where $k_{c||}(B)=\mu_0 J_{c||}(B)/B$. Flux redistribution occurs when $|J_{\perp}|$ ($|J_{||}|$) exceeds $J_{c\perp}$ ($J_{c||}$), in which case $E_{\perp}\neq 0$ ($E_{||}\neq 0$).

For simplicity we take $J_{c\perp}$ and $k_{c||}$ to be constants independent of $B$. In our calculations, the critical profiles of $B$ and $\alpha$ then obey

$$\frac{\partial B}{\partial x}=\pm B_0/x_0 \tag{12}$$

and

$$\frac{\partial\alpha}{\partial x}=\pm k_{c||} \ , \tag{13}$$

where $x_0=B_0/\mu_0 J_{c\perp}=\text{const}$. We define $\chi=k_{c||}x_0=J_{c||}(B_0)/J_{c\perp}$ and $\mu=k_{c||}x_m$.

## III. DIAMAGNETIC INITIAL STATE

We begin a more detailed discussion of the behavior in a rotating applied field by considering first the simplest case, the time evolution from a diamagnetic initial state. At $t=0$, the flux-density distribution in the superconductor is given by $\mathbf{B}(x,0)=\hat{\mathbf{z}}B_0(1-x/x_0)$ for $x\leq x_0$ and $\mathbf{B}(x,0)=0$ for $x>x_0$. Here $B_0$ is the magnitude of the applied magnetic field and $x_0=B_0/\mu_0 J_{c\perp}$ is the distance from the surface at which $B$ is reduced from $B_0$ to zero.

As $\alpha_s(t)$ slowly increases from zero, the distribution of $\mathbf{B}$ predicted by Eqs. (1)—(13) initially develops the two-zone structure shown in Fig. 1: a $C_-T_+$ zone $[0\leq x<x_c(t)]$ in which both flux-line cutting and transport occur, and an $O$ zone ($x_c\leq x<x_m$) in which neither flux-line cutting nor flux transport occurs.

In the region $C_-T_+$, where $x_c(t)=\alpha_s(t)/k_{c||}$, the vortex structure is at both the flux-line-cutting and the depinning thresholds, such that $\alpha(x,t)=\alpha_s(t)-k_{c||}x$, $J_{||}(x,t)=-k_{c||}B(x,t)/\mu_0$, and $J_{\perp}=J_{c\perp}$. The solutions of Eqs. (7) and (8), subject to $E_{||}(x_c,t)=E_{\perp}(x_c,t)=0$ are

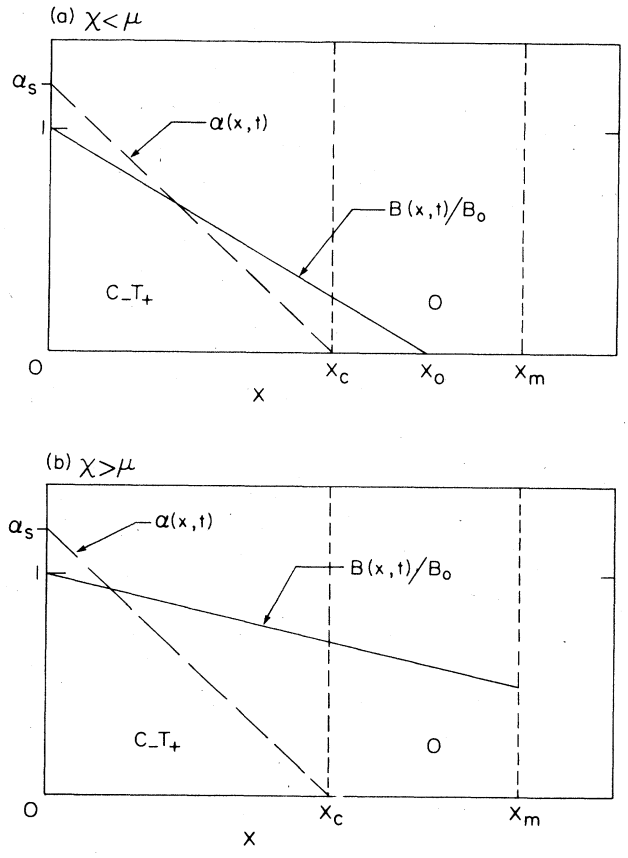


FIG. 1. Two-zone structure [$C_-T_+$-$O$] evolving from the diamagnetic initial state. (a) $\chi=k_{c||}x_0<\mu=k_{c||}x_m$, (b) $\chi>\mu$.

$$E_{||}(x,t)=-\frac{\omega B_0}{k_{c||}}\left[\left[1-\frac{x_c}{x_0}\right]\sin[k_{c||}(x_c-x)]+\frac{1}{\chi}\{1-\cos[k_{c||}(x_c-x)]\}\right], \quad (14)$$

$$E_{\perp}(x,t)=\frac{\omega B_0}{k_{c||}}\left[\left[1-\frac{x}{x_0}\right]-\left[1-\frac{x_c}{x_0}\right]\cos[k_{c||}(x_c-x)]-\frac{1}{\chi}\sin[k_{c||}(x_c-x)]\right]. \quad (15)$$

As $\alpha_s$ increases, the altered-**B** region grows, and we obtain the sequence of profiles of $B(x,t)$ and $\alpha(x,t)$ sketched in Fig. 2. The electric fields of Eqs. (14) and (15) satisfy the conditions $E_{||}(x,t)\leqq 0$ and $E_{\perp}(x,t)\geqq 0$ throughout the region $0\leqq x\leqq x_c(t)$ only for limited values of $\alpha_s$ and $\chi$. The range of validity corresponds to regions $A$ and $B$ of Fig. (I.1),[6] but with $\mu$ replaced by $\alpha_s=k_{c||}x_c$ in Eq. (I.17).[6] If $\alpha_s$ and $\chi$ are within these ranges, a quasisteady-state distribution of **B** is achieved when either $x_c=x_0$ ($\alpha_s=\chi=k_{c||}x_0$) for $x_0<x_m$ [Figs. 1(a) and 2(a)] or when $x_c=x_m$ ($\alpha_s=\mu=k_{c||}x_m$) for $x_0>x_m$ [Figs. 1(b) and 2(b)]. In the former case, the behavior after reaching the quasisteady state is given by Eqs. (I.18)—(I.20), which describe region $A$ of Fig. (I.1); in the latter case, the behavior is given by Eqs. (I.21)—(I.23), which describe region $B$ of Fig. (I.1).

For values of $\alpha_s$ and $\chi$ outside the above ranges, this theory predicts time-dependent instabilities similar to flux jumps. The resulting behavior can be described in terms of moving $C$ and $CT$ zones, which move so fast that eddy currents and the possibility of thermal runaway must be taken into account. Space does not permit a discussion of such behavior in this paper.

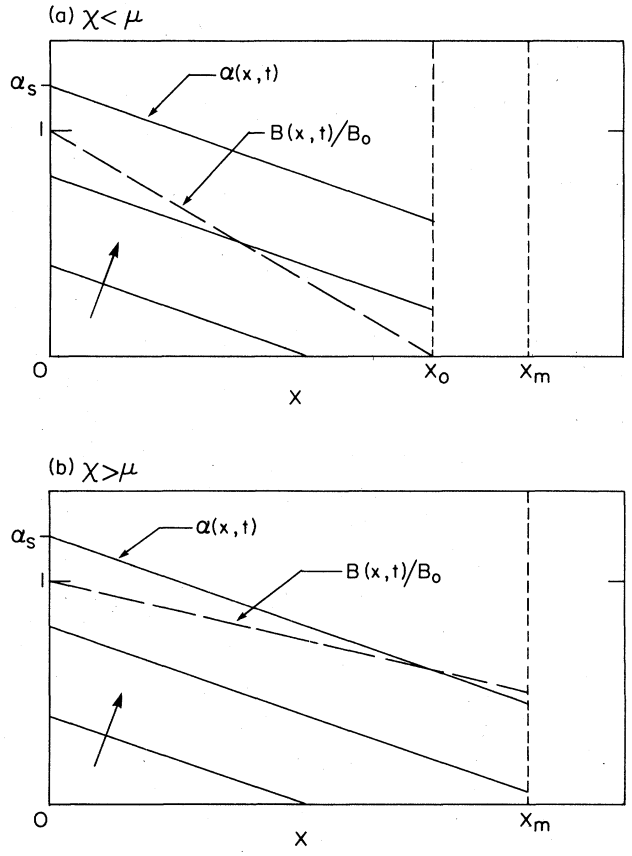


FIG. 2. Time evolution of $B(x,t)$ and $\alpha(x,t)$ starting from the diamagnetic initial state. (a) $\chi<\mu$, (b) $\chi>\mu$.

## IV. PARAMAGNETIC INITIAL STATE

For a paramagnetic initial state we have the following conditions at $t=0$: $B(x,0)=B_0(1+x/x_0)$, as shown by the uppermost dashed line in Fig. 3, and $\alpha(x,0)=0$.

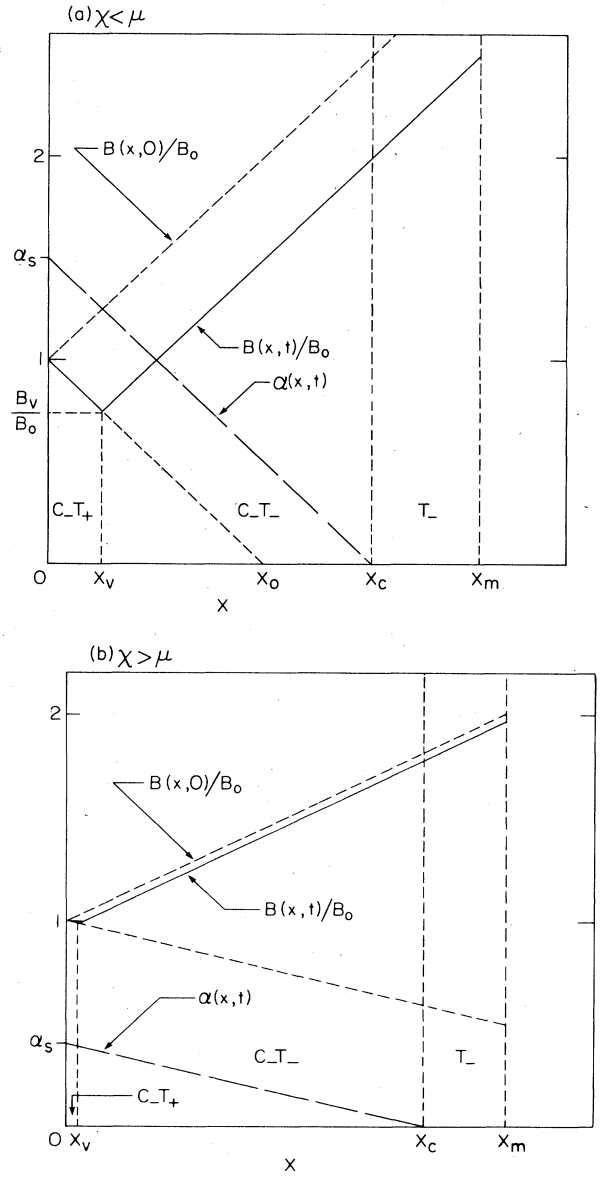


FIG. 3. Three-zone structure [$C_-T_+/C_-T_-T_-$] evolving from the paramagnetic initial state for $x_c<x_m$. (a) $\chi<\mu$: here, $\chi=1$, $\mu=k_{c||}x_m=2$, and $\alpha_s=k_{c||}x_c=1.5$; (b) $\chi>\mu$: here, $\chi=1$, $\mu=0.5$, and $\alpha_s=0.406$.

As $\alpha_s(t)$ increases from zero, Eqs. (1)—(13) predict initially the three-zone structure sketched in Fig. 3: a $C_-T_+$ zone in which flux-line cutting and flux transport to the right occur, a $C_-T_-$ zone in which flux-line cutting and flux transport to the left occur, and a $T_-$ zone in which only flux transport to the left occurs. The vortices in the entire specimen are at the depinning threshold, and they are at the onset of flux-line cutting in the region $0 \leqq x < x_c$. The solutions of Eqs. (7) and (8), subject to the conditions $E_{\parallel}(x_c)=0$, $E_{\perp}(x_m)=0$, and $E_{\perp}(x_v)=0$, are as follows.

Region $C_-T_+$ $[0 \leqq x < x_v(t)]$:

$$E_{\parallel}(x,t)=-\frac{\omega B_0}{k_{c\parallel}}\left[\left[1-\frac{x_v}{x_0}\right]\sin[k_{c\parallel}(x_v-x)]+\frac{1}{\chi}\{1-(\tilde{E}_{\parallel}^{v}+1)\cos[k_{c\parallel}(x_v-x)]\}\right], \tag{16}$$

$$E_{\perp}(x,t)=\frac{\omega B_0}{k_{c\parallel}}\left[\left[1-\frac{x}{x_0}\right]-\left[1-\frac{x_v}{x_0}\right]\cos[k_{c\parallel}(x_v-x)]-\frac{1}{\chi}(\tilde{E}_{\parallel}^{v}+1)\sin[k_{c\parallel}(x_v-x)]\right]. \tag{17}$$

Region $C_-T_-$ $[x_v(t) \leqq x < x_c(t)]$:

$$E_{\parallel}(x,t)=-\frac{\omega B_0}{k_{c\parallel}}\left\{\left[1-2\frac{x_v}{x_0}+\frac{x_c}{x_0}+\left[\frac{x_m}{x_0}-\frac{x_c}{x_0}\right]\frac{d\theta_v}{d\alpha_s}\right]\sin[k_{c\parallel}(x_c-x)]-\frac{1}{\chi}\left[1-2\frac{d\theta_v}{d\alpha_s}\right]\{1-\cos[k_{c\parallel}(x_c-x)]\}\right\}, \tag{18}$$

$$E_{\perp}(x,t)=\frac{\omega B_0}{k_{c\parallel}}\left\{\left[1-2\frac{x_v}{x_0}+\frac{x}{x_0}\right]+\frac{1}{\chi}\left[1-2\frac{d\theta_v}{d\alpha_s}\right]\sin[k_{c\parallel}(x_c-x)]-\left[1-2\frac{x_v}{x_0}+\frac{x_c}{x_0}+2\left[\frac{x_m}{x_0}-\frac{x_c}{x_0}\right]\frac{d\theta_v}{d\alpha_s}\right]\cos[k_{c\parallel}(x_c-x)]\right\}. \tag{19}$$

Region $T_-$ $[x_c(t) \leqq x \leqq x_m]$:

$$E_{\parallel}(x,t)=0\,, \tag{20}$$

$$E_{\perp}(x,t)=-2\frac{\omega B_0}{k_{c\parallel}}\left[\frac{x_m}{x_0}-\frac{x}{x_0}\right]\frac{d\theta_v}{d\alpha_s}\,. \tag{21}$$

In the above,

$$\tilde{E}_{\parallel}^{v}=-\frac{(2\chi-3\theta_v+\mu)(1-\cos\alpha_v)+(\alpha_s-\mu)(\theta_v-\chi)\sin\alpha_v}{\sin\alpha_v-(\alpha_s-\mu)\cos\alpha_v}\,, \tag{22}$$

and $\theta_v$ is the solution of

$$\frac{d\theta_v}{d\alpha_s}=\frac{\chi-\theta_v+\sin(\alpha_s-\theta_v)-(\chi-2\theta_v+\alpha_s)\cos(\alpha_s-\theta_v)}{2\sin(\alpha_s-\theta_v)-2(\alpha_s-\mu)\cos(\alpha_s-\theta_v)} \tag{23}$$

with initial condition $\theta_v=0$ at $\alpha_s=0$. We have used the following for Eqs. (22) and (23): $\theta=k_{c\parallel}x$, $\chi=k_{c\parallel}x_0$, $\mu=k_{c\parallel}x_m$, $\theta_v=k_{c\parallel}x_v$, $\alpha_s=k_{c\parallel}x_c$, and $\alpha_v=\alpha_s-\theta_v$.

The $B$ and $\alpha$ profiles are given by

$$B=B_0(1-x/x_0),\quad 0 \leqq x < x_v\ (C_-T_+) \tag{24a}$$

$$B=B_0(1-2x_v/x_0+x/x_0)\,,\quad x_v \leqq x < x_m\ (C_-T_-\text{ and }T_-) \tag{24b}$$

and

$$\alpha=\alpha_s-k_{c\parallel}x,\quad 0 \leqq x < x_c\ (C_-T_+\text{ and }C_-T_-) \tag{25a}$$

$$\alpha=0,\quad x_c \leqq x < x_m\ (T_-)\,. \tag{25b}$$

If $x_0 < x_m$ [Fig. 3(a)], and $x_v$ reaches $x_0$ while $x_c < x_m$, the specimen enters the quasisteady state with a frozen core of thickness $2(x_m-x_0)$ around $x_m$, and a diamagnetic shoulder of thickness $x_0$ at each surface.

On the other hand, if $x_c$ reaches $x_m$ before $x_v=x_0$ for $x_0 < x_m$ [Fig. 3(a)], or when $x_c=x_m$ for $x_0 > x_m$ [Fig. 3(b)], the specimen goes from the three-zone behavior just described to the two-zone structure of Fig. 4. Flux-line cutting occurs throughout the entire sample; in addition, transport to the right occurs in the $C_-T_+$ zone $(0 \leqq x < x_v)$, and transport to the left occurs in the $C_-T_-$ zone $(x_v \leqq x \leqq x_m)$. In this case, the boundary conditions are $E_{\parallel}(x_m)=E_{\perp}(x_m)=0$ and $E_{\perp}(x_v)=0$, and the solutions of Eqs. (7) and (8) are as follows.

Region $C_-T_+$ $[0 \leqq x < x_v(t)]$: $E_{\parallel}(x,t)$ and $E_{\perp}(x,t)$ are given by Eqs. (16) and (17), with $\tilde{E}_{\parallel}^{v}$ given not by Eq. (22) but by

$$\tilde{E}_{\parallel}^{v}=-\frac{(2\chi-3\theta_v+\mu)[1-\cos(\mu-\theta_v)]}{\sin(\mu-\theta_v)}\,, \tag{26}$$

where $\theta_v$ is the solution of

$$\frac{d\theta_v}{d\alpha_s}=\frac{\chi-\theta_v+\sin(\mu-\theta_v)-(\chi-2\theta_v+\mu)\cos(\mu-\theta_v)}{2\sin(\mu-\theta_v)} . \tag{27}$$

The initial conditions for Eq. (27) are $\alpha_s=\mu$ and $\theta_v=\theta_{v0}$, where $\theta_{v0}$ is obtained from Eq. (23) when $\alpha_s=\mu$.

Region $C_-T_-$ $[x_v(t)\leqq x\leqq x_m]$:

$$E_{||}(x,t)=-\frac{\omega B_0}{k_{c||}}\left[\left[1-2\frac{x_v}{x_0}+\frac{x_m}{x_0}\right]\sin[k_{c||}(x_m-x)]-\frac{1}{\chi}\left[1-2\frac{d\theta_v}{d\alpha_s}\right]\{1-\cos[k_{c||}(x_m-x)]\}\right] , \tag{28}$$

$$E_{\perp}(x,t)=\frac{\omega B_0}{k_{c||}}\left[\left[1-2\frac{x_v}{x_0}+\frac{x}{x_0}\right]+\frac{1}{\chi}\left[1-2\frac{d\theta_v}{d\alpha_s}\right]\sin[k_{c||}(x_m-x)]-\left[1-2\frac{x_v}{x_0}+\frac{x_m}{x_0}\right]\cos[k_{c||}(x_m-x)]\right] . \tag{29}$$

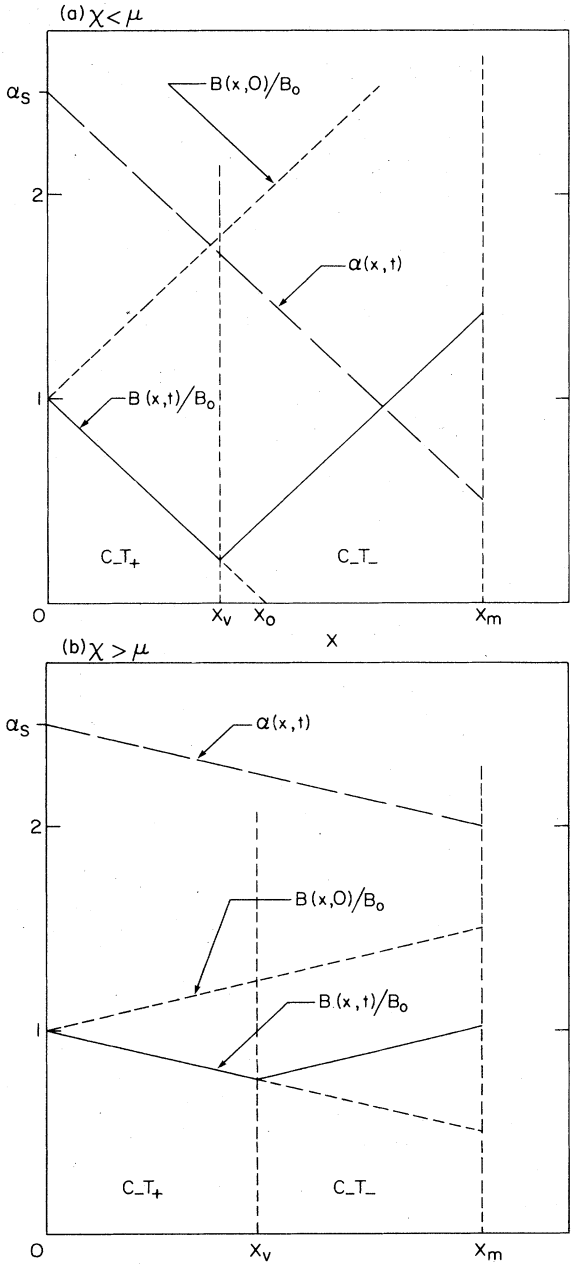


FIG. 4. Two-zone structure $[C_-T_+/C_-T_-]$ evolving from the paramagnetic initial state for $x_c>x_m$. The sample parameters are the same as in Fig. 3, except that $\alpha_s=2.5$. (a) $\chi<\mu$, (b) $\chi>\mu$.

For $x_0<x_m$ [Fig. 4(a)], the specimen enters the quasisteady state when $x_v=x_0$, and again it has a frozen core and a diamagnetic shoulder. For $x_0\geqq x_m$ [Fig. 4(b)], we obtain from Eq. (27) the surprising result that the quasisteady state, in which $x_v=x_m$, is not achieved for finite $\alpha_s$. On the other hand, $x_v$ very closely approaches $x_m$ for large $\alpha_s$. As $\alpha_s\to\infty$, Eq. (27) yields

$$x_m-x_v\propto\alpha_s^{-1},\quad x_0=x_m,\ \chi=\mu , \tag{30a}$$

$$x_m-x_v\propto\exp[-(\chi-\mu)\alpha_s/4],\quad x_0>x_m,\ \chi>\mu . \tag{30b}$$

Figure 5 gives several examples of this behavior. Shown are plots of $\theta_v=k_{c||}x_v$ versus $\alpha_s$ for $\mu=k_{c||}x_m=1$ and various values of $\chi=k_{c||}x_0$. For $\chi=0.5$ and $\chi=0.75$, the sample enters the quasisteady state when $\theta_v=\chi$ as in Fig. 4(a). On the other hand, for $\chi=1$ and $\chi=2$, $\theta_v$ approaches $\mu$ asymptotically from below, as expected from Eqs. (30). When $x_0\geqq x_m$ and $\alpha_s\gg1$, the specimen has a diamagnetic shoulder that extends from the surface to almost the center of the specimen.

## V. NONMAGNETIC INITIAL STATE

We assume that at $t=0$ the flux density in the superconductor is uniform $[\mathbf{B}(x,0)=B_0\hat{\mathbf{z}}]$ and equal to the applied field. We first consider the case for which the specimen is sufficiently thick that, during the approach to the quasisteady state, the regions of altered **B**, **J**, and **E** do not penetrate as far as the center of the slab.

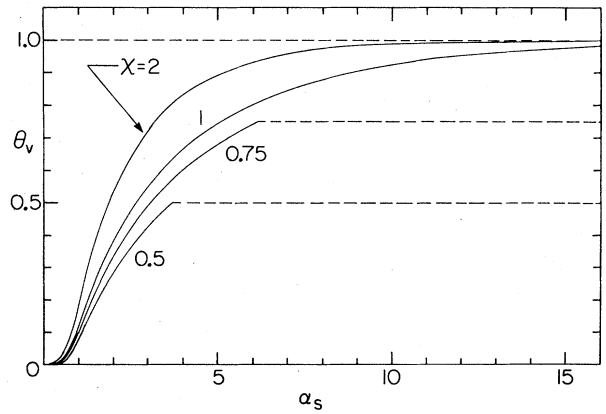


FIG. 5. $\theta_v=k_{c||}x_v$ versus $\alpha_s$ for $\mu=k_{c||}x_m=1$ and $\chi=k_{c||}x_0=0.5$, 0.75, 1.0, and 2.0, as computed from Eq. (27).

### A. Initial three-zone structure [$C_-T_+/C_-$-$O$]

As $\alpha_s(t)$ slowly increases from zero, the distribution predicted by Eqs. (1)—(13) initially develops the three-zone structure sketched in Fig. 6. A $V$-shaped minimum in $B(x,t)$ versus $x$ occurs at $x=x_v(t)$, where $B(x_v,t)=B_v(t)=B_0[1-x_v(t)/x_0]$. To the left of the minimum is a zone $C_-T_+$ $[0\leqq x<x_v(t)]$ in which both flux-line cutting and transport occur. To the right of the minimum are a zone $C_-$ $[x_v(t)\leqq x<x_c(t)]$ in which only flux-line cutting occurs and a zone $O$ $[x_c(t)\leqq x\leqq x_m]$ in which $B(x,t)=B_0$, $\alpha(x,t)=0$, and neither flux-line cutting nor flux transport occurs.

The vortex structure is at the flux-line-cutting threshold throughout the region $0\leqq x\leqq x_c(t)$, where $x_c(t)=\alpha_s(t)/k_{c\|}$, such that $\alpha(x,t)=\alpha_s(t)-k_{c\|}x$ and $J_\|(x,t)=-k_{c\|}\times B(x,t)/\mu_0$. The vortex structure in region $C_-$ $[x_v(t)\leqq x<x_c(t)]$ is below the depinning threshold, such that $|J_\perp|<J_{c\perp}$ and $E_\perp=0$. In this region the solutions of Eqs. (7) and (8), subject to $B(x_c,t)=B_0$ and $E_\perp(x_c,t)=0$, are

$$E_\|(x,t)=-\frac{\omega B_0}{k_{c\|}}\sin[k_{c\|}(x_c-x)]\ , \tag{31}$$

$$B(x,t)=B_0\cos[k_{c\|}(x_c-x)]\ , \tag{32}$$

where $\omega=d\alpha_s/dt$. Thus, Eq. (6) yields

$$J_\perp(x,t)=-J_{c\perp}\chi\sin[k_{c\|}(x_c-x)]\ . \tag{33}$$

Continuity of $B(x,t)$ at $x=x_v(t)$ yields

$$\theta_v(t)=k_{c\|}x_v(t)=\chi(1-\cos\alpha_v)\ , \tag{34}$$

where

$$\alpha_v=\alpha(x_v,t)=\alpha_s(t)-\theta_v(t)\ .$$

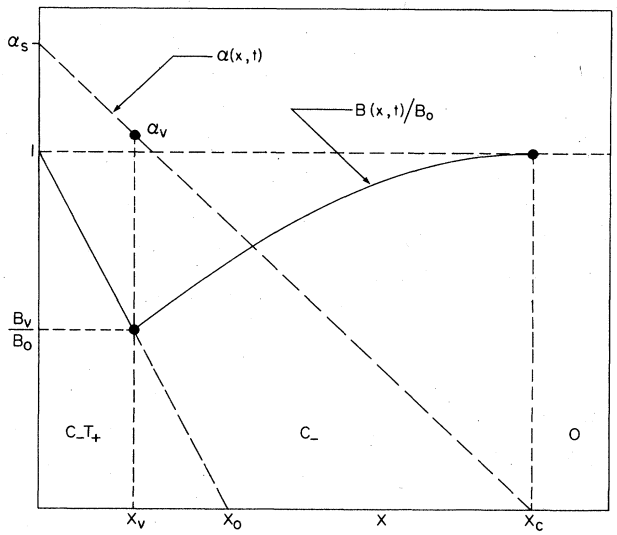


FIG. 6. Initial three-zone structure [$C_-T_+/C_-$-$O$] evolving from the nonmagnetic initial state for $\chi<1$. For this plot, $\chi=0.5$ and $\alpha_s=1.297$.

In the region $C_-T_+$ $[0\leqq x<x_v(t)]$ the vortices are at the depinning threshold, such that $|J_\perp|=J_{c\perp}$ and $B(x)=B_0(1-x/x_0)$. The solutions of Eqs. (7) and (8), subject to $E_\perp(x_v,t)=0$ and

$$E_\|(x_v,t)=-(\omega B_0/k_{c\|})\sin\alpha_v\ ,$$

are

$$E_\|(x,t)=-\frac{\omega B_0}{k_{c\|}}\left[\sin[k_{c\|}(x_c-x)]+\frac{1}{\chi}\{1-\cos[k_{c\|}(x_v-x]\}\right]\ , \tag{35}$$

$$E_\perp(x,t)=\frac{\omega B_0}{k_{c\|}}\left[\left[1-\frac{x}{x_0}\right]-\cos[k_{c\|}(x_c-x)]-\frac{1}{\chi}\sin[k_{c\|}(x_v-x)]\right]\ . \tag{36}$$

These quantities obey $E_\|(x,t)\leqq 0$ and $E_\perp(x,t)\geqq 0$ throughout the region $0\leqq x\leqq x_v(t)$.

The initial three-zone structure of Fig. 6 and the corresponding Eqs. (31)—(36) apply only in limited regions of values of $\alpha_s$ and $\chi$. Consider first the behavior when $\chi\leqq 1$. As $\alpha_s$ increases, $x_c$, the front of the altered-**B** region, penetrates more deeply into the superconductor, and the sequence of profiles of $B(x,t)$ and $\alpha(x,t)$ sketched in Fig. 7 occurs. Equations (31)—(36) remain valid, provided $\alpha_s=k_{c\|}x_c<\eta_1(\chi)$, where

$$\eta_1(\chi)=\chi+\pi/2\ . \tag{37}$$

The value of $B_v$ is reduced to zero and a quasisteady-state distribution of $B$ is achieved when $\alpha_s=k_{c\|}x_c=\eta_1(\chi)$ [Figs. 7(a) and 7(b), curves $d$]. For $\alpha_s>\eta_1(\chi)$ (Fig. 8), no further changes in $B$ occur, but $\alpha(x,t)=\alpha_s(t)-k_{c\|}x$ within a distance $x_0$ of the surface [Fig. 7(b), curve $e$]. The behavior then is given by Eqs. (I.21)—(I.23), which describe region $A$ of Fig. (I.1).

However, when $\chi>1$, Eqs. (31)—(36) apply only as long as $|J_\perp(x,t)|<J_{c\perp}$ in the region $x_v(t)\leqq x<x_c(t)$. From Eq. (33) we see that, for $\chi>1$, this condition is first violated when $\sin[\alpha_v(t)]=1/\chi$ or $\alpha_s=k_{c\|}x_c=\eta_2(\chi)$, where

$$\eta_2(\chi)=\sin^{-1}(1/\chi)+\chi-(\chi^2-1)^{1/2}\ . \tag{38}$$

This function, plotted in Fig. 8, has the limiting values $\eta_2(1)=\pi/2+1=2.57$ and $\eta_2(\chi)\cong 3/2\chi$ for $\chi\gg 1$. For $\alpha_s>\eta_2(\chi)$, the following structure occurs.

### B. Four-zone structure [$C_-T_+/C_-T_-$-$C_-$-$O$]

For $\chi>1$ and $\alpha_s=k_{c\|}x_c>\eta_2(\chi)$, the distribution of **B** predicted by Eqs. (1)—(13) changes from that of Fig. 6 into that of Fig. 9. The minimum value of $B(x,t)$ occurs at $x=x_v(t)$, where

$$B(x_v,t)=B_v(t)=B_0[1-x_v(t)/x_0]\ .$$

To the left of the minimum is a zone $C_-T_+$ $[0\leqq x<x_v(t)]$ in which both flux-line cutting and transport occur. To the right of the minimum are three zones:

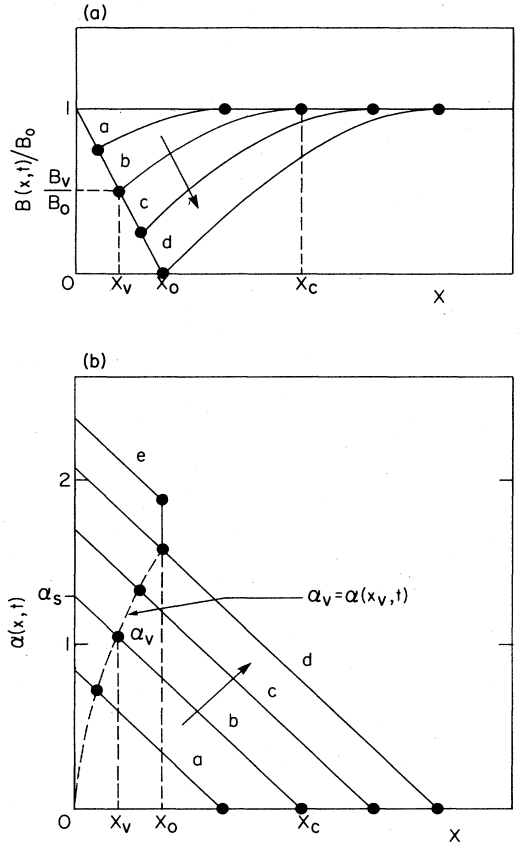


FIG. 7. Time evolution of (a) $B(x,t)$ and (b) $\alpha(x,t)$ from the nonmagnetic initial state in the initial three-zone structure. Sample parameters are as in Fig. 6. Here $\eta_1(\chi)=2.071$ and, for curves $a,b,c$, and $d$, respectively, $\alpha_s=0.848$, 1.297, 1.693, and $2.071=\eta_1(\chi)$, where the quasisteady state is achieved (Sec. V A). For $\alpha_s>2.071$ no further changes in $B$ occur, but $\alpha$ varies within $x_0$ from the surface as shown in curve $e$. Values of $B_v/B_0$, $x_v$, $x_c$, and $\alpha_s$ are labeled for curves $b$. The dashed curve shows $\alpha(x_v,t)$.

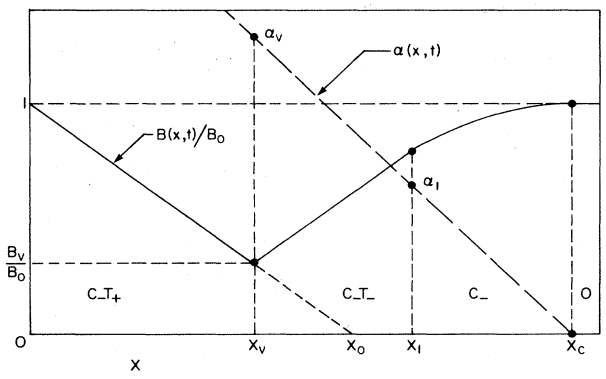


FIG. 9. Four-zone structure $[C_-T_+/C_-T_-C_-O]$ evolving from the nonmagnetic initial state for $1<\chi<1.70$. Here, $\chi=1.3$, $\alpha_s=2.187$.

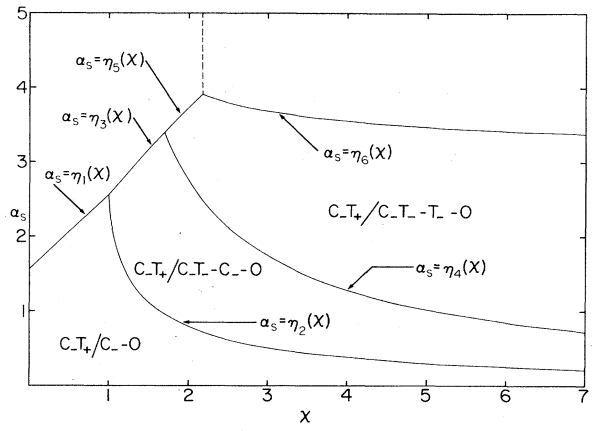


FIG. 8. Evolving multiple-zone structures predicted by Eqs. (28)—(47) for increasing $\alpha_s$, starting from the nonmagnetic initial state. For $\chi<1$ the specimen first develops a $[C_-T_+/C_-O]$ structure and then achieves the quasisteady state when $\alpha_s=\eta_1(\chi)$. For $1<\chi<1.7$, the sample starts with a $[C_-T_+/C_-O]$ structure for $\alpha_s<\eta_2(\chi)$, develops a $[C_-T_+/C_-T_-C_-O]$ structure for $\eta_2(\chi)<\alpha_s<\eta_3(\chi)$, and reaches the quasisteady state when $\alpha_s=\eta_3(\chi)$. For $1.7<\chi\lesssim 2.16$, the sample has a $[C_-T_+/C_-O]$ structure for $\alpha_s<\eta_2(\chi)$, a $[C_-T_+/C_-T_-C_-O]$ structure for $\eta_2(\chi)<\alpha_s<\eta_4(\chi)$, and a $[C_-T_+/C_-T_-T_-O]$ structure for $\eta_4(\chi)<\alpha_s<\eta_5(\chi)$. It achieves the quasisteady state when $\alpha_s=\eta_5(\chi)$. For $\chi>2.16$, the specimen passes through the same zone structures as in the latter case, but instead of reaching the quasisteady state, the behavior becomes unstable when $\alpha_s=\eta_6(\chi)$. The details of this behavior are not treated here.

a zone $C_-T_-$ $[x_v(t)\leqq x<x_1(t)]$ in which both flux-line cutting and flux transport occur, a zone $C_-$ $[x_1\leqq x<x_c(t)]$ in which only flux-line cutting occurs, and a zone $O$ $[x_c(t)\leqq x\leqq x_m]$ in which $B(x,t)=B_0$, $\alpha(x,t)=0$, and neither flux-line cutting nor flux transport occurs.

Throughout the region $0\leqq x<x_c(t)$, the vortex structure is at the flux-line-cutting threshold, such that $\alpha(x,t)=\alpha_s(t)-k_{c\|}x$ and $J_\|(x,t)=-k_{c\|}B(x,t)/\mu_0$. The vortex structure in region $C_-$ $[x_1(t)\leqq x<x_c(t)]$ is below the depinning threshold, such that $|J_\perp|<J_{c\perp}$, $E_\perp=0$, and $E_\|(x,t)$, $B(x,t)$, and $J_\perp(x,t)$ are given by Eqs. (31)—(33).

The vortex structure in the region $C_-T_-$ $[x_v(t)\leqq x<x_1(t)]$ is at the depinning threshold, such that $J_\perp=-J_{c\perp}$ and

$$B(x,t)=B_0[1+x/x_0-2x_v(t)/x_0]\,. \tag{39}$$

The solutions of Eqs. (7) and (8), subject to $E_\perp(x_1,t)=0$ and $E_\|(x_1,t)=-(\omega B_0/k_{c\|})\sin\alpha_1$, where $\alpha_1(t)=\alpha(x_1,t)$, are

$$E_{||}(x,t)=-\frac{\omega B_0}{k_{c||}}\left[\sin[k_{c||}(x_c-x)]-\frac{1}{\chi}\left[1-2\frac{d\theta_v}{d\alpha_s}\right]\{1-\cos[k_{c||}(x_1-x)]\}\right], \tag{40}$$

$$E_{\perp}(x,t)=\frac{\omega B(x,t)}{k_{c||}}-\frac{\omega B_0}{k_{c||}}\left[\cos[k_{c||}(x_c-x)]-\frac{1}{\chi}\left[1-2\frac{d\theta_v}{d\alpha_s}\right]\sin[k_{c||}(x_1-x)]\right], \tag{41}$$

which obey $E_{||}(x,t)\leqq 0$ and $E_{\perp}(x,t)\leqq 0$ in zone $C_-T_-$. Continuity of $B$ at $x=x_1$ yields, from Eqs. (32) and (39),

$$\theta_v=\{\theta_1+\chi[1-\cos(\alpha_s-\theta_1)]\}/2\ , \tag{42}$$

where $\theta_1=k_{c||}x_1$ and $\theta_v=k_{c||}x_v$. Because $E_{\perp}(x,t)\geqq 0$ in region $C_-T_+$, we must have $E_{\perp}(x_v,t)=0$, which in combination with Eqs. (41) and (42) yields

$$\frac{d\theta_1}{d\alpha_s}=1+\frac{\chi[1-\cos(\alpha_s-\theta_v)]-\theta_v}{[1-\chi\sin(\alpha_s-\theta_1)]\sin(\theta_1-\theta_v)}\ . \tag{43}$$

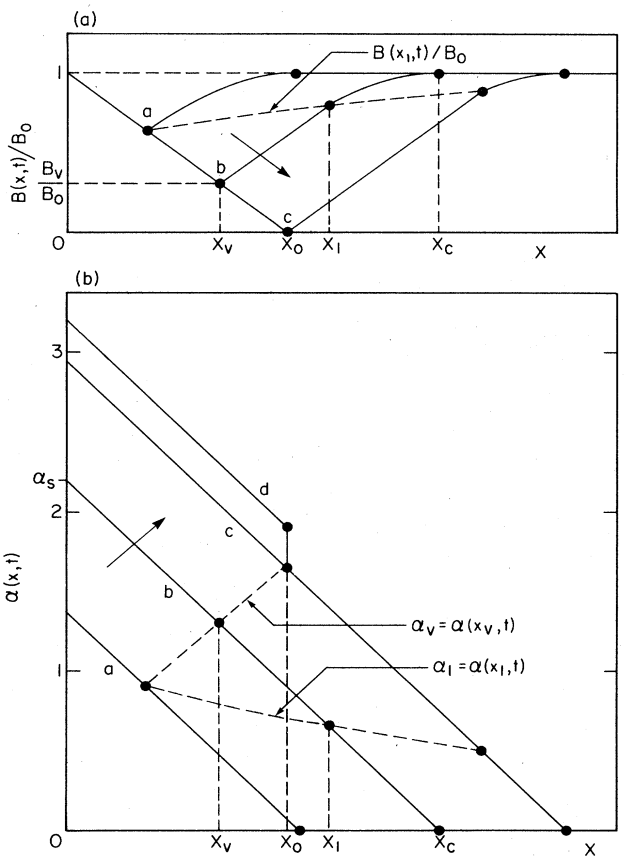


FIG. 10. Four-zone-structure $[C_-T_+/C_-T_--C_--O]$ time evolution of (a) $B(x,t)$ and (b) $\alpha(x,t)$ from the nonmagnetic initial state for $1<\chi\leqq 1.70$ and increasing $\alpha_s$. For this plot, $\chi=1.3$, $\eta_2(\chi)=1.347$, and, for curves $a,b$, and $c$, respectively, $\alpha_s=k_{c||}x_c=1.347=\eta_2(\chi)$, $\alpha_s=0.187$, and $\alpha_s=2.931=\eta_3(\chi)$, where the quasisteady state (Sec. V B) is achieved. [For $\alpha_s<1.347=\eta_2(\chi)$, the $B$ and $\alpha$ structure is as in Fig. 6.] For $\alpha_s>2.931$, no further changes in $B$ occur, but $\alpha$ varies within $x_0$ of the surface as shown by curve $d$. Values of $B_v/B_0$, $x_v$, $x_1$, $x_c$, and $\alpha_s$ are labeled for curves $b$. The dashed curves show $B(x_1,t)/B_0$, $\alpha(x_v,t)$, and $\alpha(x_1,t)$.

Numerical solutions of this equation, subject to the boundary conditions that $\theta_1=\theta_v=\chi-(\chi^2-1)^{1/2}$, $d\theta_1/d\alpha_s=1.309\,017$, and $d\theta_v/d\alpha_s=\frac{1}{2}$ at $\alpha_s=\eta_2(\chi)$, give $\theta_1=k_{c||}x_1$, $\theta_v=k_{c||}x_v$, and $B_v/B_0=(1-\theta_v/\chi)$ as functions of $\alpha_s=k_{c||}x_c$.

The four-zone structure $[C_-T_+/C_-T_--C_--O]$ of Fig. 9 and the corresponding Eqs. (39)—(43) apply only in limited regions of values of $\alpha_s$ and $\chi$. Consider first the case for which $1<\chi\leqq 1.70$. As $\alpha_s$ increases beyond $\eta_2(\chi)$, which causes $x_c$ to penetrate more deeply into the superconductor, the sequence of profiles of $B(x,t)$ and $\alpha(x,t)$ sketched in Fig. 10 occurs. Equations (39)—(43) apply provided $\eta_1(\chi)\leqq\alpha_s\leqq\eta_3(\chi)$, where $\eta_3$ is defined as the value of $\alpha_s$ at which the solutions of Eq. (43) yield $\theta_v=\chi$ or $B_v=0$. The quasisteady-state distribution of $B$ is thus achieved when $\alpha_s=k_{c||}x_c=\eta_3(\chi)$ (see Fig. 10, curves $c$). Numerically obtained values of $\eta_3(\chi)$ over the range $1<\chi\leqq 1.70$, shown in Fig. 8, are approximated with an error of less than 0.3% by

$$\eta_3(\chi)\cong 2.571+1.186(\chi-1)\ . \tag{44}$$

For $\alpha_s>\eta_3(\chi)$, no further changes in $B$ occur, but $\alpha(x,t)=\alpha_s(t)-k_{c||}x$ within a distance $x_0$ of the surface, as shown in Fig. 10(b), curve $d$. The behavior then is given by Eqs. (I.21)—(I.23).

When $\chi>1.70$, however, Eqs. (39)—(43) apply only for $\alpha_s<\eta_4(\chi)$, where $\eta_4(\chi)$ is the value of $\alpha_s$ at which the solutions of Eq. (43) yield $\theta_1=\alpha_s$ and $\theta_v=\alpha_s/2<\chi$. Numerically obtained values of $\eta_4(\chi)$, shown in Fig. 8, can be approximated over the range $1.70<\chi<7$ with an error of less than 2% by

$$\eta_4(\chi)\cong\eta_2(\chi)+(3.35+0.93/\chi)\sin^{-1}(1/\chi)\ . \tag{45}$$

For $\alpha_s>\eta_4(\chi)$ the following structure occurs.

### C. Four-zone structure $[C_-T_+/C_-T_--T_--O]$

For $\chi>1.70$ and $\alpha_s=k_{c||}x_c>\eta_4(\chi)$, the distribution of B predicted by Eqs. (1)—(13) changes from that of Fig. 9 into that of Fig. 11. The minimum value of $B(x,t)$ occurs at $x=x_v(t)$, where

$$B(x_v,t)=B_v(t)=B_0[1-x_v(t)/x_0]\ .$$

To the left of the minimum is a zone $C_-T_+$ $[0\leqq x<x_v(t)]$ in which $B=B_0(1-x/x_0)$, and both flux-line cutting and transport occur. To the right of the minimum there are three more zones: a zone $C_-T_-$ $[x_v(t)\leqq x<x_c(t)]$ in which both flux-line cutting and transport occur, a zone $T_-$ $[x_c(t)\leqq x<x_1(t)]$ in which only flux transport occurs, and a zone $O$ $[x_1(t)\leqq x\leqq x_m]$ in which $B(x,t)=B_0$, $\alpha(x,t)=0$, and neither flux-line cutting nor flux transport occurs.

Throughout the region $x_v(t)\leqq x<x_1(t)$, the vortex

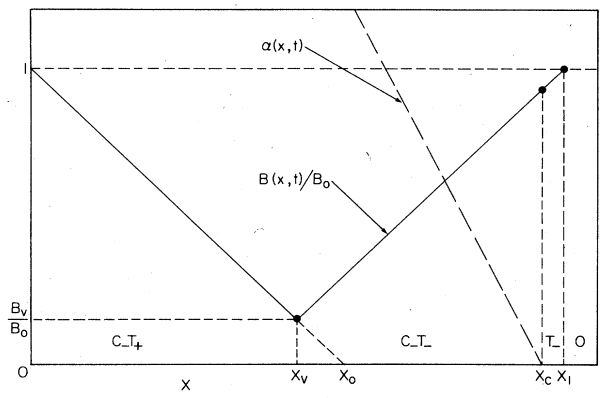


FIG. 11. Four-zone structure $[C\_T_+/C\_T\_\text{-}T\_\text{-}O]$ evolving from the nonmagnetic initial state for $1.70<\chi<2.16$. Here, $\chi=2$ and $\alpha_s=3.25$.

structure is at the depinning threshold such that $J_\perp=-J_{c\perp}$ and $B(x,t)$ is given by Eq. (39) or, since $x_1(t)=2x_v(t)$, by

$$B(x,t)=B_0\{1+[x-x_1(t)]/x_0\} . \tag{46}$$

Because no flux-line cutting occurs in zone $T\_$ $[x_c(t)\leqq x<x_1(t)]$, the solutions of Eqs. (7) and (8) are $E_{||}(x,t)=0$ and

$$E_\perp(x,t)=-\frac{\omega B_0}{\chi}\frac{d\theta_1}{d\alpha_s}[x_1(t)-x] . \tag{47}$$

The vortex structure in the region $C\_T\_$ $[x_v(t)\leqq x<x_c(t)]$ is at the flux-line-cutting threshold, such that $\alpha(x,t)=\alpha_s-k_{c||}x$. The solutions of Eqs. (7) and (8), subject to $E_{||}(x_c,t)=0$ and

$$E_\perp(x_c,t)=-(\omega B_0/\chi)(d\theta_1/d\alpha_s)[x_1(t)-x_c(t)] ,$$

are

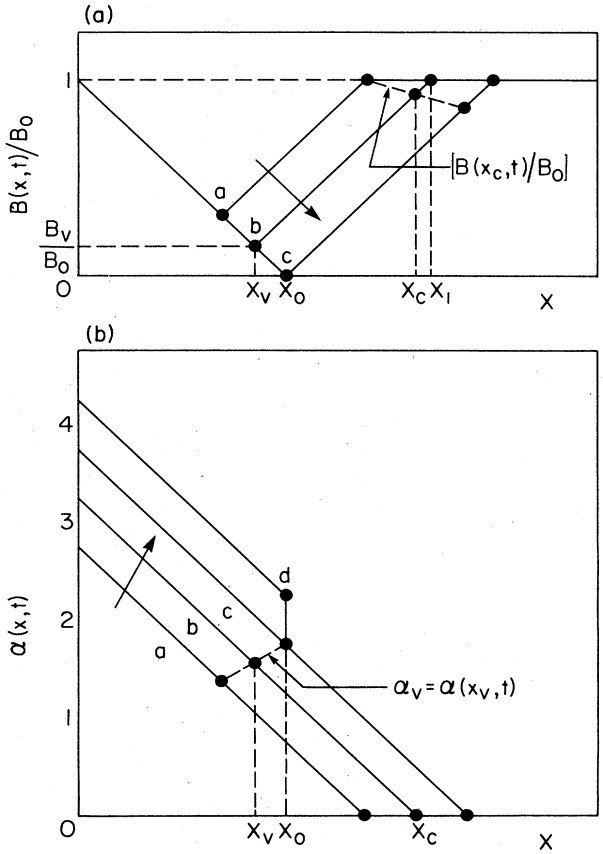


FIG. 12. Four-zone-structure $[C\_T_+/C\_T\_\text{-}T\_\text{-}O]$ time evolution of (a) $B(x,t)$ and (b) $\alpha(x,t)$ from the nonmagnetic initial state for $1.70<\chi<2.16$. For this plot $\chi=2$, and, for curves $a,b$, and $c$, respectively, $\alpha_s=2.75=\eta_4(\chi)$, $\alpha_s=3.25$, and $\alpha_s=3.724=\eta_5(\chi)$, where the quasisteady state is achieved (Sec. V C). [For $\alpha_s<0.791=\eta_2(\chi)$, the $B$ and $\alpha$ structure is as in Fig. 6, and for $0.791<\alpha_s<2.75=\eta_4(\chi)$, the $B$ and $\alpha$ structure is as in Fig. 9.] For $\alpha_s>3.724$ no further changes in $B$ occur, but $\alpha$ varies within $x_0$ of the surface as shown in curve $d$. The dashed curves show $B(x_c,t)/B_0$ and $\alpha(x_v,t)$.

$$E_{||}(x,t)=-\frac{\omega B_0}{k_{c||}}\left\{\left[1+\frac{1}{\chi}\left[\frac{d\theta_1}{d\alpha_s}-1\right](\theta_1-\alpha_s)\right]\sin[k_{c||}(x_c-x)]+\frac{1}{\chi}\left[\frac{d\theta_1}{d\alpha_s}-1\right]\{1-\cos[k_{c||}(x_c-x)]\}\right\} , \tag{48}$$

$$E_\perp(x,t)=-\frac{\omega}{k_{c||}}\left[\frac{B_0}{\chi}\left[\frac{d\theta_1}{d\alpha_s}-1\right]\left[(\theta_1-\alpha_s)\cos[k_{c||}(x_c-x)]+\sin[k_{c||}(x_c-x)]\right]-B(x,t)+B_0\cos[k_{c||}(x_c-x)]\right] , \tag{49}$$

which obey $E_{||}(x,t)\leqq 0$ and $E_\perp(x,t)\leqq 0$ in zone $C\_T\_$. Because $E_\perp(x,t)\geqq 0$ in zone $C\_T_+$, we must have $E_\perp(x_v,t)=0$, such that Eq. (49) yields

$$\frac{d\theta_1}{d\alpha_s}=\frac{\chi-\theta_v+(\theta_1-\alpha_s-\chi)\cos(\alpha_s-\theta_v)+\sin(\alpha_s-\theta_v)}{(\theta_1-\alpha_s)\cos(\alpha_s-\theta_v)+\sin(\alpha_s-\theta_v)} , \tag{50}$$

where $\theta_v=k_{c||}x_v=\theta_1/2$. Numerical solutions of this equation, subject to the boundary condition at $\alpha_s=\eta_4(\chi)$ [see curve $\eta_4(\chi)$ in Fig. 8] that $\alpha_s=2\theta_v=\theta_1=\eta_4(\chi)$, give $\theta_1=k_{c||}x_1$, $\theta_v=k_{c||}x_v$, and $B_v/B_0=(1-x_v/x_0)$ as functions of $\alpha_s=k_{c||}x_c$. The time evolution of the multiple-zone structure is illustrated in Fig. 12.

As in other cases, this four-zone structure only applies for limited values of $\alpha_s$ and $\chi$. As $\alpha_s$ increases to values larger than $\eta_4(\chi)$, the sample can reach either the quasisteady state or an unstable state, depending upon the value of $\chi$. For $1.70<\chi<2.16$, the sequence of profiles shown in Fig. 12 occurs: For $\eta_4(\chi)<\alpha_s<\eta_5(\chi)$, Eqs. (46)–(50) are valid, and the sample reaches the quasisteady state when $\alpha_s=\eta_5(\chi)$, which is the value of

$\alpha_s(t)$ such that $B_v=0$. The function $\eta_5(\chi)$, shown in Fig. 8, must be obtained numerically from Eq. (50). For $\chi>2.16$, Eqs. (46)—(50) apply only for $\eta_4(\chi)\leqq\alpha_s\leqq\eta_6(\chi)$, where $\eta_6(\chi)$ is the value of $\alpha_s$ for which $E_{||}(x=0)=0$. The function $\eta_6(\chi)$ shown in Fig. 8, must be obtained numerically from Eq. (50) while monitoring $E_{||}(0,t)$ using Eq. (48). For $\alpha_s>\eta_6(\chi)$, dynamical instabilities develop, and the sample cannot be treated quasistatically with the present theory.

In the above discussion we have considered only the behavior when the sample is sufficiently thick that the regions of altered **B** do not penetrate to the center of the slab. If this condition is not met, we must change from the boundary conditions used above to those in which the electric field is zero in the middle of the slab $[E_{||}(x_m)=E_{\perp}(x_m)=0]$ when a zone of altered **B** reaches the slab center. The precise behavior depends upon whether $x_c$ first reaches $x_m$ in the three-zone structure $[C\_T_+/C\_\text{-}O]$ of Fig. 6 or in the four-zone structure $[C\_T_+/C\_T\_\text{-}C\_\text{-}O]$ of Fig. 9, or whether $x_1$ reaches $x_m$ in the four-zone structure $[C\_T_+/C\_T\_\text{-}T\_\text{-}O]$ of Fig. 11. There are too many different cases to discuss in detail here. The resulting magnetic structures, however, all can be determined from analytic or numerical solutions of Eqs. (1)—(13).

## VI. SUMMARY AND CONCLUSIONS

In this paper we have used the general critical-state theory of Ref. 1 to calculate the time dependence of the magnetic induction **B** (magnitude $B$ and angle $\alpha$) during the approach to the quasisteady state for a type-II superconducting slab subjected to a magnetic field which is parallel to the slab's flat surfaces and which changes in direction but not in magnitude. This theory contains two important material-dependent quantities: $J_{c\perp}$, the transverse critical current density, and $k_{c||}=\mu_0 J_{c||}/B$, where $J_{c||}$ is the parallel critical current density. Our calculations were done beginning with three different initial magnetic states: diamagnetic (Sec. III), paramagnetic (Sec. IV), and nonmagnetic (Sec. V). In every case we have shown that, regardless of magnetic history, flux-line cutting consumes $B$, ultimately taking the sample to a final, quasisteady magnetic state in which $B$ has a diamagnetic profile either in a region near the surface or in the entire sample, depending upon sample thickness and flux-line-pinning strength. In applying this theory we have assumed, for simplicity, that $J_{c\perp}=$const and $k_{c||}=$const. The resulting profiles of $B$ and $\alpha$ yield results in qualitative agreement with most of the experimental findings of Refs. 2—4.

Although our theory is similar in several respect to the empirical model of Refs. 2—4, there are important differences in both the physical interpretation and the details of the $B$ and $\alpha$ profiles. Both models assume (a) that the steepest metastable gradients of $B$ are given by $|\partial B/\partial x|=\mu_0 J_{c\perp}$, regardless of whether $B$ is changing direction or not, and (b) that the steepest metastable gradients of $\alpha$ are given by $|\partial\alpha/\partial x|=k_{c||}$. According to the empirical model,[3] on the one hand, "if the initial magnetic induction $B_i(x)$ exceeds the value $B(x)$ established in the quasisteady state, then flux lines, somehow, *escape* from the disk during the rotation leading to setting up the quasisteady state." This model[3] also "implies that flux can exit from the specimen although the magnetic pressure or Lorentz force in the surface region is directed inwards." Our theory, on the other hand, provides a mechanism, flux-line cutting, which reduces $B$ in the specimen's interior and leads to diamagnetic profiles near the surface. The reduction of $B$ is a natural consequence of Faraday's law, which, when written as Eq. (1), states that when flux-line cutting occurs, $B$ is not conserved but is irreversibly consumed. According to our theory, flux lines do *not* migrate *out* of the specimen against a flux density gradient. Instead, as the diamagnetic profiles are being established at the surface, flux transport *into* the specimen occurs, but this only partially replenishes the $B$ that is consumed via flux-line cutting.

According to our theory, the details of the evolving $B$ and $\alpha$ profiles (Figs. 1—12) are considerably more complex than those proposed in Refs. 2—4, and this complexity is required to satisfy both Faraday's law [Eqs. (7) and (8)] and continuity of **E** as a function of $x$. The main difference between our profiles and those of Refs. 2—4 are as follows.

(a) Relative to the changing $B$ profiles, our changing $\alpha$ profiles penetrate more deeply into the specimen than those assumed in Refs. 2—4. The differences show up most clearly in a comparison of Figs. 6 and 7 and 9—12 with Figs. 3(a) and 3(b) of Ref. 4, which exhibits profiles that we claim are inconsistent with Faraday's law and continuity of **E** versus $x$.

(b) In addition to zones common to both models, in which (i) both the $B$ and $\alpha$ gradients are critical, (ii) only the $B$ gradient is critical, or (iii) both the $B$ and $\alpha$ gradients are subcritical, our theory predicts zones in which only the $\alpha$ gradient is critical. In such $C$ zones no flux transport occurs, but flux-line-cutting processes reduce $B$ at a rate given by Eq. (1).

In this paper we have kept the $B$ dependences of $J_{c||}$ and $J_{c\perp}$ as simple as possible in order to obtain analytical expressions for the various fields involved and to illustrate the main features of the $B$ and $\alpha$ profiles. For detailed comparisons of theoretical and experimental results, however, particularly when the applied field varies over a wide range, more realistic $B$ dependences of $J_{c||}$ and $J_{c\perp}$ will have to be included, which in turn will require numerical solutions of Eqs. (1)—(11). We have developed a computer program to incorporate these changes, as well as to compute hysteretic losses. We shall present our method and results in a subsequent publication. We have found that this numerical approach helps greatly in understanding the complex behavior that occurs when the field applied at the surface varies not only in direction but also in magnitude.

## ACKNOWLEDGMENTS

We are grateful to Dr. M. A. R. LeBlanc, Dr. J. R. Cave, Dr. R. Boyer, and Dr. G. Fillion for stimulating discussions and correspondence. Ames Laboratory is operated for the U.S. Department of Energy by Iowa State University under Contract No. W-7405-Eng-82. This work was supported by the Director for Energy Research, Office of Basic Energy Sciences.

[1]J. R. Clem and A. Perez-Gonzalez, Phys. Rev. B **30**, 5041 (1984).
[2]R. Boyer and M. A. R. LeBlanc, Solid State Commun. **24**, 261 (1977).
[3]R. Boyer, G. Fillion, and M. A. R. LeBlanc, J. Appl. Phys. **51**, 1692 (1980).
[4]J. R. Cave and M. A. R. LeBlanc, J. Appl. Phys. **53**, 1631 (1982).
[5]J. R. Clem, Phys. Rev. B **26**, 2463 (1982). See this paper, which reviews the current theoretical and experimental situation, for numerous references to related work.
[6]The symbol I in equation or figure numbers, e.g., Eq. (I.17), denotes equations or figures of Ref. 1.